Cu^+ transient species mediate Cu catalyst reconstruction during CO_2 electroreduction

Jan Vavra[a], Federico Dattila[b], Attila Kormányos[c], Serhiy Cherevko[c], Núria Lopéz[b], Raffaella Buonsanti[a*]

[a]*Laboratory of Nanochemistry for Energy (LNCE), Institute of Chemical Sciences and Engineering (ISIC), École Polytechnique Fédérale de Lausanne, CH-1950 Sion, Switzerland.*

[b]*Institute of Chemical Research of Catalonia (ICIQ), The Barcelona Institute of Science and Technology (BIST), Tarragona, Spain*

[c]*Helmholtz-Institute Erlangen-Nürnberg for Renewable Energy (IEK-11), Forschungszentrum Jülich, Cauerstrasse 1, 91058 Erlangen, Germany*

*Correspondence to: raffaella.buonsanti@epfl.ch

Abstract

Understanding metal surface reconstruction during operation is of the uttermost importance in heterogeneous catalysis as it directly affects the available active sites. However, surface reconstruction is notoriously difficult to study because of the dynamic nature of the phenomena behind it. Here, we report on the mechanism and the intermediates, which drive the rearrangement of copper catalysts during the electrochemical CO_2 reduction reaction. In-situ methods, including mass spectrometry and fluorescence spectroscopy, evidence a dissolution – redeposition process mediated by transient species containing copper in +1 oxidation state. Theory identifies copper-adsorbate complexes which form in solution under operating conditions. Copper carbonyls and oxalates emerge as the major reaction-specific species driving copper reconstruction. This work motivates future studies to specifically target these compounds to improve the catalyst operational stability in the electrochemical CO_2 reduction reaction.

Introduction

A growing interest in sustainable production of chemicals and fuels accompanies the current shift to renewable energy. The electrochemical CO_2 reduction reaction (CO_2RR) is a promising approach to convert waste CO_2 into value added products, such as ethylene or ethanol.[1] Copper is typically used to catalyze the reaction and a great progress has been made in understanding the parameters which govern its activity and selectivity.[1,2] Numerous studies show that the arrangement of Cu surface atoms has profound effect on performance.[3–5] Yet, evidences pile up for the dynamic nature of Cu surfaces under CO_2RR conditions, despite metallic Cu being supposedly stable at the cathodic potentials of CO_2RR. [6–13] Fundamental understanding of these dynamic processes is essential for the implementation of this technology from the catalyst to a device level, which targets high selectivity and long-term stability.

Copper dissolves transiently during the formation of surface oxides and during oxide reduction to metallic copper.[14-17] As a result, Cu catalyst reconstruction is often associated with these redox processes. [14–16] These events occur at potentials close to the open circuit potential (OCP) of a typical CO_2RR experiment, which is around $+0.4V_{RHE}$ (RHE = Reversible Hydrogen Electrode).[17] The catalyst typically encounters OCP during the cell assembly and electrolyte introduction or during a start/stop operation. During the cell startup, where the working electrode experiences cathodic potentials, the redeposition of the Cu ions dissolved at OCP occurs and induces changes in the catalyst morphology and total exposed surface.[14–16] The OCP conditions can be avoided with an auxiliary cell controlling the cathode potential when the catalyst is introduced in the electrolyte or during a start-stop operation. In fact, the application of a cathodic potential during the cell assembly was proven essential to preserve the activity of Cu nanocatalysts smaller than 10 nm.[18]

Various evidence suggests that the Cu catalyst reconstruction continues under reducing potential during CO_2RR. A study based on in-situ X-ray absorption and diffraction showed changes in surface coordination of Cu atoms in response to the applied potential.[19] Electrochemical scanning probe microscopy revealed that Cu foil reconstructs not only during the start/stop cycle, but also under continuous cathodic bias. [6,20,21] The reconstruction of small Cu spheres was recently monitored by in-situ liquid-phase transmission electron microscopy (TEM), where a dissolution – redeposition mechanism was proposed to drive their structural evolution.[14] The presence of dissolved Cu intermediates in the proximity of the electrode is required to mediate the proposed reconstruction process.

Here, these intermediate species are identified via complexation with an organic ligand which prolongs their lifetime, allowing their in-situ detection. Experimental evidence demonstrates that these transient species contain copper in the +1 oxidation state. Density Functional Theory (DFT) identifies these species as copper carbonyls and copper oxalates. These molecules are adsorbed intermediates of the CO_2RR which enable transient dissolution of Cu by forming coordination complexes with Cu^+ ions even at the cathodic potentials of CO_2RR.

Results

Catalyst characterization

To investigate the transient species mediating the Cu catalyst reconstruction during CO_2RR, a model system of ~ 7nm Cu spheres was chosen (Fig. 1A). The small nanoparticles (NPs) expose a large surface area to the electrolyte and possess relatively high number of undercoordinated atoms on their high-curvature surface. These features account for rapid and irreversible structural transformations in the initial phases of CO_2RR.[7,9,12] Such short timescales ease the study of the phenomena related to their reconstruction. Furthermore, the low size polydispersity of these Cu NPs is beneficial to form 2D self-assembled monolayers on the surface of the glassy carbon supporting electrode (Fig. 1B), which was utilized to repeatedly create consistent films with an optimized dip-coating protocol (see Experimental Section for details). Indeed, the measured electrochemically active surface area (ECSA) of the electrodes was reproducible to within 10% (Supplementary Fig. S1.1). The as-synthesized NPs consist of mostly metallic Cu, as evidenced by electron diffraction (Fig. 1C). Here, the observed reflections match with Cu fcc structure. A minor contribution of Cu_2O to the diffraction signal is observed, most visible as a shoulder at 4 nm^{-1} corresponding to Cu_2O {111} reflection.

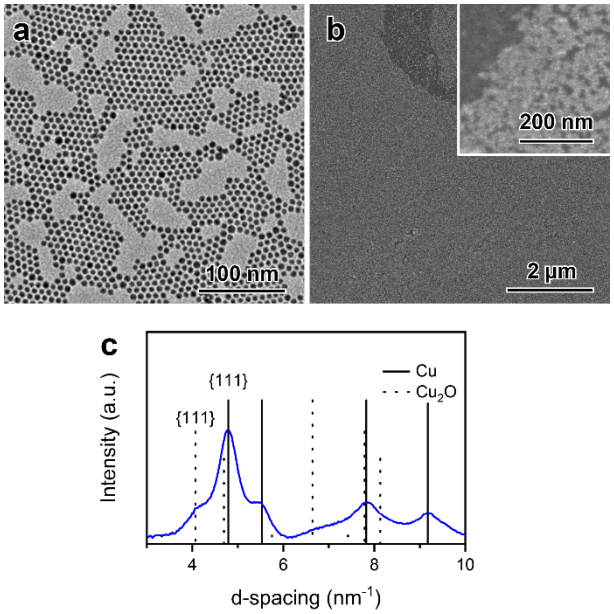

Fig. 1: Characterization of the as-synthesized Cu catalyst. (a) TEM image of the as-synthesized Cu spheres with mean size of around 7 nm; (b) Scanning electron microscopy (SEM) of the Cu spheres deposited on a glassy carbon electrode via dip-coating. The inset shows the (sub)monolayer catalyst packing. (c) Electron diffraction of the as-synthesized catalyst evidencing the metallic nature of the sample. Reflections are assigned to the Cu fcc structure.

The Cu NPs undergo severe reconstruction in the first minutes of CO2RR and characteristic Cu_2O cubes are observed by post-mortem analysis (Supplementary Fig. S1.2). This behavior is consistent with literature reports.[9,12,22] In-situ liquid-phase TEM has suggested that this reconstruction occurs via a dissolution – redeposition mechanism mediated by dissolved Cu species.[14] As the dissolution and redeposition occur simultaneously, it is imperative to use highly sensitive detection methods to capture the Cu transient species.

Dissolved Cu detected with on-line ICP-MS

A scanning electrochemical flow cell coupled to an inductively coupled plasma mass spectrometer (on-line ICP-MS) was used to detect the amount of the dissolved species. This system is extremely sensitive and capable of detecting pg cm^{-2} amounts of dissolved Cu ions.[23,24] The dissolution rate of copper is reported as a function of time with the applied current and measured potential (Fig. 2) The cell was operated in chronopotentiometric mode (CP). A low negative baseline current (–0.28 mA cm^{-2}) was applied to the working electrode during the

immersion in the electrolyte. This protocol prevents the catalyst exposure to OCP, where Cu oxidizes and dissolves (Supplementary Fig. S2.1). Pulses at progressively more negative currents (from –0.55 mA cm^{-2} to –4.4 mA cm^{-2}) were applied for a gradually more extended time (between 20 – 55 s) to simulate the CO_2RR conditions (Fig. 2a). Concomitantly, a progressively more negative potential was measured (Fig.2b). After each pulse, both the current and the potential return to the baseline. The reported CP profile is a result of parameter optimization (details in the Supplementary Note S2.1)

In the immersion step, the measured potential is cathodic compared to the reduction potential of Cu_2O to Cu^0, which is around 0.1 V_{RHE} (Fig. 2b, blue curve). Thus, only a small contact dissolution feature is observed (Fig. 2c, blue curve), which is likely related to surface rearrangements during the reduction of a thin layer of native oxide.[25] No dissolution is detected after that until the last pulse, where the potential reaches –1.1 V_{RHE} (Fig. 2b, blue curve). Following this pulse, a small dissolution signal, close to the detection limit, emerges at 1200s (Fig. 2c, blue curve). Overall, ICP-MS does not detect much Cu in solution. This observation suggests that the soluble Cu species responsible for Cu catalyst reconstruction are short lived and confined to the vicinity of the working electrode. In other words, under the investigated regimes, the redeposition of intermediates occur at a rate that faster or at least comparable to the rate of their generation.

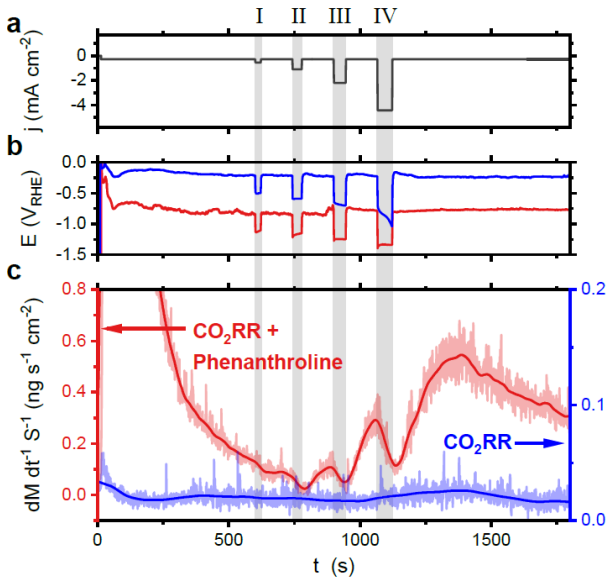

Fig. 2: On-line ICP-MS measuring the dissolution rate of Cu NPs under cathodic bias. (a) Optimized protocol for the applied current: contact with the electrolyte was established while

applying –0.28 mA cm^{-2}; after a 600s hold at this current density, four current pulses separated by 120s with gradually decreasing current densities were applied: pulse I (–0.55 mA cm^{-2} for 20 s), pulse II (–1.1 mA cm^{-2} for 35s), pulse III (–2.2 mA cm^{-2} for 45s) and pulse IV (–4.4 mA cm^{-2} for 55 s). (b) Measured cell potential. It is noted that the measured potentials in the presence of phenanthroline are more negative, further discussion is in SI Section 3. (c) Cu mass dissolution rate. 0.05 M $KHCO_3$ saturated with CO_2 was used as the electrolyte. Phenanthroline was added to the electrolyte (1 mM) to prolong the lifetime of the Cu intermediate species. Data acquired without and with the phenanthroline are reported in blue and red, respectively. Dissolution curves were denoised using a Locally Weighted Scatterplot Smoothing (LOWESS) filter. For the sake of clarity; the original data are presented behind the smoothed curves (pale blue and red curves).

Phenanthroline is known to strongly coordinate Cu ions.[26–28] Thus, this molecule was introduced in the electrolyte to prolong the lifetime of these intermediates and enable their reliable detection. Indeed, the presence of the phenanthroline greatly amplified the Cu dissolution signal.

Both the contact dissolution and dissolution during the pulsed operation are now clearly discerned above the baseline (Fig 2c, red curve). A sharp onset at time zero is observed for the contact dissolution peak, with maximum intensity detected within a few seconds after contact and then it slowly decays back to the baseline. This profile corresponds to a significant dissolution event followed by rinsing/flushing of the dissolved Cu intermediates via the electrolyte flow. During the current pulses, the dissolution profile changes appreciably. The signal decreases for the duration of the negative current pulse and starts to increase when the current returns to its baseline. The intensity of the signal reaches its maximum value around 200 s after the most negative pulse at -1.1V_{RHE} and decreases afterwards. Similar behavior of that described for the Cu NPs was observed for Cu foil (Supplementary Fig. S2.2 and S2.3), thus proving that the measured cathodic Cu dissolution is intrinsic to Cu as a material, and does not originate from nanoparticle detachment or any other phenomena specific to the nanoparticles.

Detection of intermediates by in-situ fluorescence

While on-line ICP-MS is a powerful method to study metal dissolution, the electrochemical flow cell operates in conditions which are different than those of the H-cell used to evaluate catalyst performance during CO_2RR. The experimental setup allows only for short cathodic pulses to prevent gas bubble nucleation, as gas bubbles would prevent reliable measurements. Furthermore, the chemical nature of the dissolved species cannot be determined by ICP-MS.

The coordination of Cu ions by phenanthroline generates a distinct fluorescence response, which offers an alternative detection principle. The fluorescent detection of metal ions with specific chelating agents is a routine technique in biology, where it enables for example intracellular detection of low concentrations of free Cu ion pools.[29–31] In the context of this study, such optical response provides a mean to localize the detection volume to close vicinity of the working electrode. With this in mind, a variant of the classical H-cell typically used in CO_2RR catalyst research was designed (Fig 3a).[32] A quartz window allows for fluorescent readout from 2 mm thick layer of electrolyte in front of the working electrode. This cell allows semi-quantitative measurements of Cu ion concentrations in a stirred, yet constant electrolyte volume of 1 ml as opposed to the constant flow of fresh electrolyte over the working electrode in the ICP-MS electrochemical cell. The static mode of operation allows for accumulation of the phenanthroline bound Cu intermediate in the catholyte, thus to overcome some of the limitations previously described.

Both Cu^+ and Cu^{2+} ions are readily coordinated by the phenanthroline, producing $[Cu(phen)_2]^+$ or $[Cu(phen)_2]^{2+}$ (Fig 3b).[26,33] The formation of these complexes can be observed and quantified in-situ, as the $[Cu(phen)_2]^+$ is a good fluorophore and its formation results in increase of the emission intensity. On the other hand, the formation of $[Cu(phen)_2]^{2+}$ complex quenches the fluorescence of the phenanthroline. To quantify the amount of dissolved Cu species in-situ, the area under an emission spectrum is integrated and compared to a calibration series with known concentration of Cu^+ or Cu^{2+} ions (Fig. 3c, additional details in the Supplementary Note S3.1). As mentioned above, the Cu reconstruction occurs via dissolution and redeposition of transient copper species. Thus, the concentration of Cu ions detected in the fluorescence set-up should be thought of as the difference between the dissolved and redeposited copper species. The measured Cu dissolution rate determined from the dissolved Cu^+ species can be then used as a metric for Cu catalyst stability.

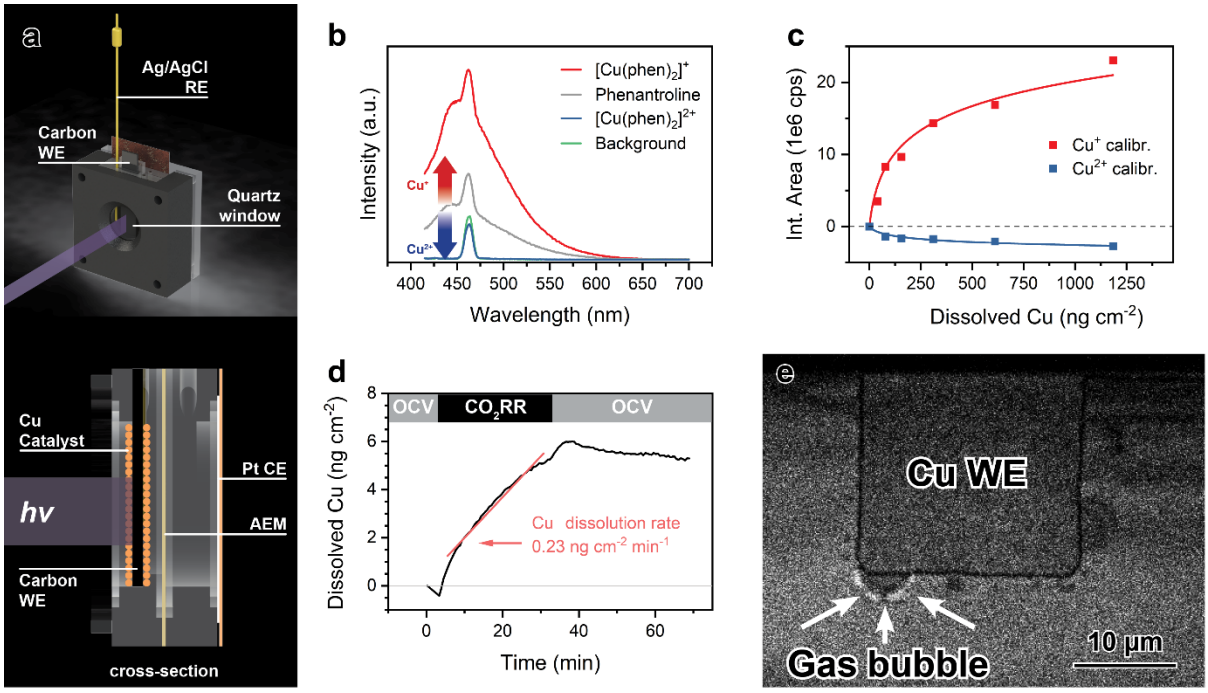

Fig. 3: Detection of the Cu intermediate species via in-situ fluorescence. (a) Sketch of the cell. The excitation beam passes a quartz window and is focused on the glassy carbon working electrode (WE), which is immersed in the catholyte. The fluorescent is detected at an angle of 170° relative to excitation beam. The potential is measured with a Ag/AgCl reference electrode (RE). The anolyte with a Pt counter electrode (CE) is separated by an anion exchange membrane (AEM). (b) Reference fluorescence emission spectra of Cu phenanthroline complexes. (c) Calibration of fluorescence intensity to a known concentration of Cu ions. (d) Representative in-situ fluorescence experiment. Dissolved Cu mass as calculated from the increase in fluorescent signal as a concentration of Cu^{+} ions. The cell is under CA operation at -0.8V_{RHE} during CO_2RR. The as-measured fluorescence intensity and electrochemical signals are reported in Supplementary Fig. S3.1. (e) In-situ fluorescence confocal microscopy resolving a bubble nucleation event (hemispherical, indicated by white arrows) on a Cu microelectrode during CO_2RR.

The results of a typical in-situ fluorescence experiment are reported as the dissolved Cu mass as a function of time (Fig 3d). As the cell is maintained at OCP for the first 5 min, there is a marked decrease in fluorescence signal, indicating formation of non-fluorescent $[Cu(phen)_2]^{2+}$ complexes. At OCP the native surface oxides dissolve as Cu^{2+} ions, this behavior is consistent with previous studies.[14–16] To simulate CO_2RR conditions, a cathodic potential of –0.8 V_{RHE} was applied between 5 min and 35 min. This is accompanied by a dramatic increase in the fluorescent signal which we assign to the release of Cu^{+} ions from the catalyst and subsequent

formation of $[Cu(phen)_2]^+$ complex. The Cu dissolution during CA is fitted with linear function and its slope, corresponds to the Cu dissolution rate during CO_2RR. When the potential returns to OCP, the fluorescence signal steadily decreases, caused mostly by catalyst dissolution to Cu^{2+} and/or spontaneous oxidation of the fluorescent $[Cu(phen)_2]^+$ complex.

Control experiments allow to confidently ascribe the signal increase to the Cu dissolution in the form of Cu^+ ions from the Cu NPs during CO_2RR. The increase in fluorescence is not originating from the electrochemical reduction of $[Cu(phen)_2]^{2+}$ complex generated at OCP. Effect of local pH on the phenanthroline fluorescence, i.e. enhanced fluorescence as a result of increased hydroxide ion concentration under CO_2RR,[34,35] was also excluded. Control experiments explaining the role of phenantroline in the system are detailed in Supplementary Note S3.2.

At first glance, the dissolution profile is different than the one measured in the ICP-MS experiment. The dissolved Cu signal steadily increases during CO_2RR in the fluorescence experiment, while it shows significant decrease in the ICP-MS experiment. The cause of the apparent disagreement likely lies in the formation of gas bubbles on the working electrode under these more realistic conditions. Gaseous products of CO_2RR generate small bubbles on the working electrode whose nucleation perturbs the dissolution – redeposition cycle in close vicinity of the electrode. This effect was visualized with the use of fluorescent confocal microscope (Fig 3e, Supplementary Fig. S3.6). Multiple bubbles are generated on the edge of a thin-film Cu microelectrode. The bright outline of the highlighted bubble corresponds to the fluorescent signal of the $[Cu(phen)_2]^+$. This observation indicates that nucleation of gas bubbles contributes to the transport of the Cu^+ containing intermediate species into bulk of the electrolyte. In the case of the on-line ICP-MS measurements, the bubble formation was deliberately minimized by applying pulsed galvanostatic protocols. Without bubbles enabling long distance transport, the Cu^+ species which form during the more negative current pulses redeposit very rapidly back onto the electrode. As the current returns to baseline values, the redeposition rate decreases, so the $[Cu(phen)_2]^+$ complex can be transported by the flowing electrolyte and detected by ICP-MS.

Operating parameters influence Cu dissolution rate

In previous studies, the occurrence of the catalytic reaction itself, the electrolyte and the effect of applied potential have been all recognized to play a role in the Cu reconstruction. [6–13] Strong binding of oxalates and carbonates has been suggested to poison the surface and may influence Cu dissolution.[36,37] Hydride-mediated cathodic corrosion mechanisms were proposed for the cathodic corrosion of noble metals. [38,39] Anomalous dissolution of Cu in acidic media under cathodic polarization was previously connected to the oxygen reduction reaction (ORR).[40–42] In addition to reaction intermediates, the cathodic bias itself contributes to the evolution of surface morphology. For instance, a joint experimental-theoretical study on graphene-covered polycrystalline copper showed that at negative potentials (< –1.0 V vs SHE), closed packed facets such as Cu(111) and Cu(100) reconstruct to more stable undercoordinated sites.[20] Grand canonical DFT simulations have also shown that Cu(100) domains loose stability in favor of Cu(111) in the presence of H and CO adsorbates and at cathodic potentials, which were identified as the driving force behind the reconstruction of Cu nanocubes.[11]

The impact of these factors on the Cu dissolution rates was studied by means of the newly developed in-situ fluorescence set-up (Fig. 4). Firstly, the effect of the applied potential was investigated at potentials between –0.8 V_{RHE} and –1.2 V_{RHE} during 30 min CA experiments (Fig 4a). The potential range was selected to cover the values typically used in CO_2RR experiments on Cu catalysts.[1] The results clearly evidence that a more cathodic potential induces a faster Cu dissolution. A 4-fold increase of dissolution rate was measured at –1.2V_{RHE} compared to the less cathodic potentials. No appreciable difference in dissolution rates or the averaged current is found between –0.8 V_{RHE} and –1.0 V_{RHE}. The measured dissolution rates scale with the current densities (Supplementary Fig S3.7), which indicates that the Cu dissolution rate is proportional to catalyst activity. Similar Cu dissolution signals were measured on larger (~44 nm) Cu cubes exposing predominantly the (100) facet or electropolished polycrystalline Cu foils (Supplementary Fig S1.3, S1.4, S3.8) demonstrating the generality of the observed Cu dissolution for Cu based CO_2RR catalysts.

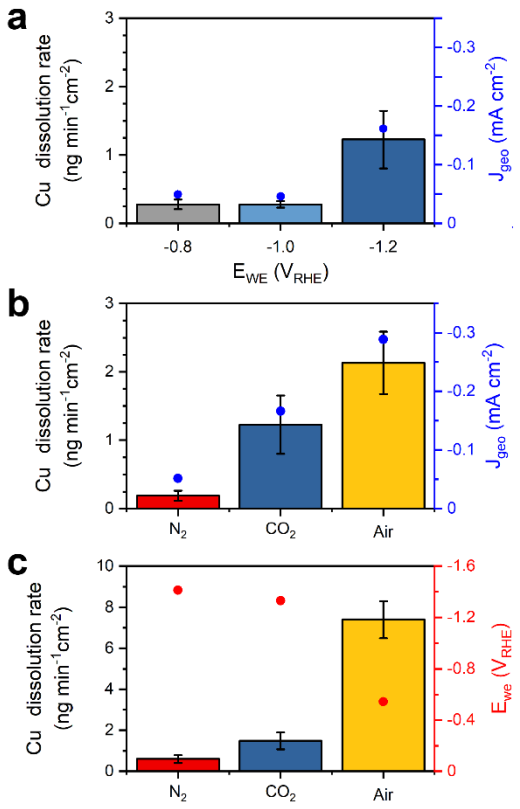

Fig. 4: Cu dissolution rates under varying reaction conditions as determined from the in-situ fluorescence experiments. (a) Influence of the potential applied in CA mode on the Cu dissolution rate; (b) Influence of gas saturation under CA conditions at –1.2 V_{RHE}. Averaged currents are reported in blue. (c) Influence of gas saturation under CP conditions at –0.16 mA cm^{-2}. Averaged potentials are reported in red. Error bars represent standard error of the mean.

The electrolyte gas saturation was then varied to investigate the influence of surface cathodic reaction on the Cu dissolution rates (Fig 4b,c). CO_2RR competes with the hydrogen evolution reaction (HER) for catalytic sites on Cu.[43,44] HER will be the dominant reaction in the absence of dissolved CO_2.[12] To look at Cu dissolution under HER conditions and in the absence of CO_2RR intermediates possibly contributing to the Cu reconstruction, the electrolyte was saturated with pure N_2 gas. It is assumed that since the nitrogen reduction reaction has large thermodynamic barrier, its rate is insignificant compared to HER under these conditions.[45]

Instead, the oxygen reduction reaction (ORR) will dominate over HER and CO_2RR if molecular oxygen is dissolved in the reaction medium, due to its lower thermodynamic and kinetic requirements.[46,47] The thermodynamic potential for ORR is +1.2 V_{RHE} , 0 V_{RHE} for the

HER and even more negative for CO_2RR. To take the possibility of Cu dissolution coupled with ORR into consideration, experiments were also conducted in air-saturated electrolyte.

Under CA operation at $-1.2V_{RHE}$ (Fig 4b), the slowest Cu dissolution rate is measured for the N_2 gas saturation. An intermediate rate of Cu dissolution is detected for the CO_2 saturation and the highest rate is observed when the electrolyte was saturated with air. As the recorded current also scales with the Cu dissolution rate, the experiments were repeated in CP mode fixing the current density at -0.16 mA cm^{-2} to decouple the effect of current density from the effect of gas saturation (Fig 4c). While the potential for N_2 saturation is the most negative at -1.5 V_{RHE}, the measured Cu dissolution rate is still appreciably smaller than for CO_2 saturation. Similarly, the dissolution rate remained the highest in air, despite the reduction in current density.

Altogether, these experiments confirm the occurrence of Cu dissolution at cathodic potentials. The results highlight that CO_2RR does accelerate this process over HER. There is a remarkable increase in the Cu dissolution rate if ORR is allowed to proceed, which occurs in the air-saturated electrolyte. Overall, the strong dependence of measured dissolution rates on surface reaction further excludes the added phenanthroline as the primary agent causing the Cu dissolution under cathodic bias.

Computational model

The identification of intermediates driving reconstruction processes in heterogeneous catalysis is difficult due to their short-lived nature.[39] Based on the experimental evidence, the hypothesized mechanism for the Cu dissolution – redeposition at cathodic potentials involves first the adsorption of CO_2, then the formation of adsorbed reaction intermediates, followed by the dissolution of metal-adsorbate complexes and eventual redeposition on the catalyst surface (Fig. 5a).

Simulations were used to assess the thermodynamics of the adsorption, formation (ΔE_{form}), dissolution (ΔE_{diss}), and redeposition processes for CO_2RR intermediates on few representative Cu facets under the cathodic potential. The DFT study was performed through the PBE functional[48] and including solvation effects through the VASPsol framework,[49,50] and explicit electric field effects, as reported in the Methods. To model the experimental system, Cu(111) (6×6), Cu(100) (6×6), and Cu(711) (1×6) were considered (Fig. 5b), respectively to assess the case of close-packed domains, open facets, and defective sites. First, DFT energies of formation

(ΔE_{form}) were obtained at U = –1.2 V_{RHE} for HER, ORR, and CO_2RR intermediates (Supplementary Fig. S4.1). Adsorbed species from the electrolyte were also included. Estimated formation energies followed well-known metal coordination based linear scaling relationships.[51–53] This initial screening indicated that *H, *OH, *CO, *OCHO and *C_2O_4 (* = adsorbed) populate the surface at –1.2 V vs RHE, thus, these adsorbates were selected for the next step.

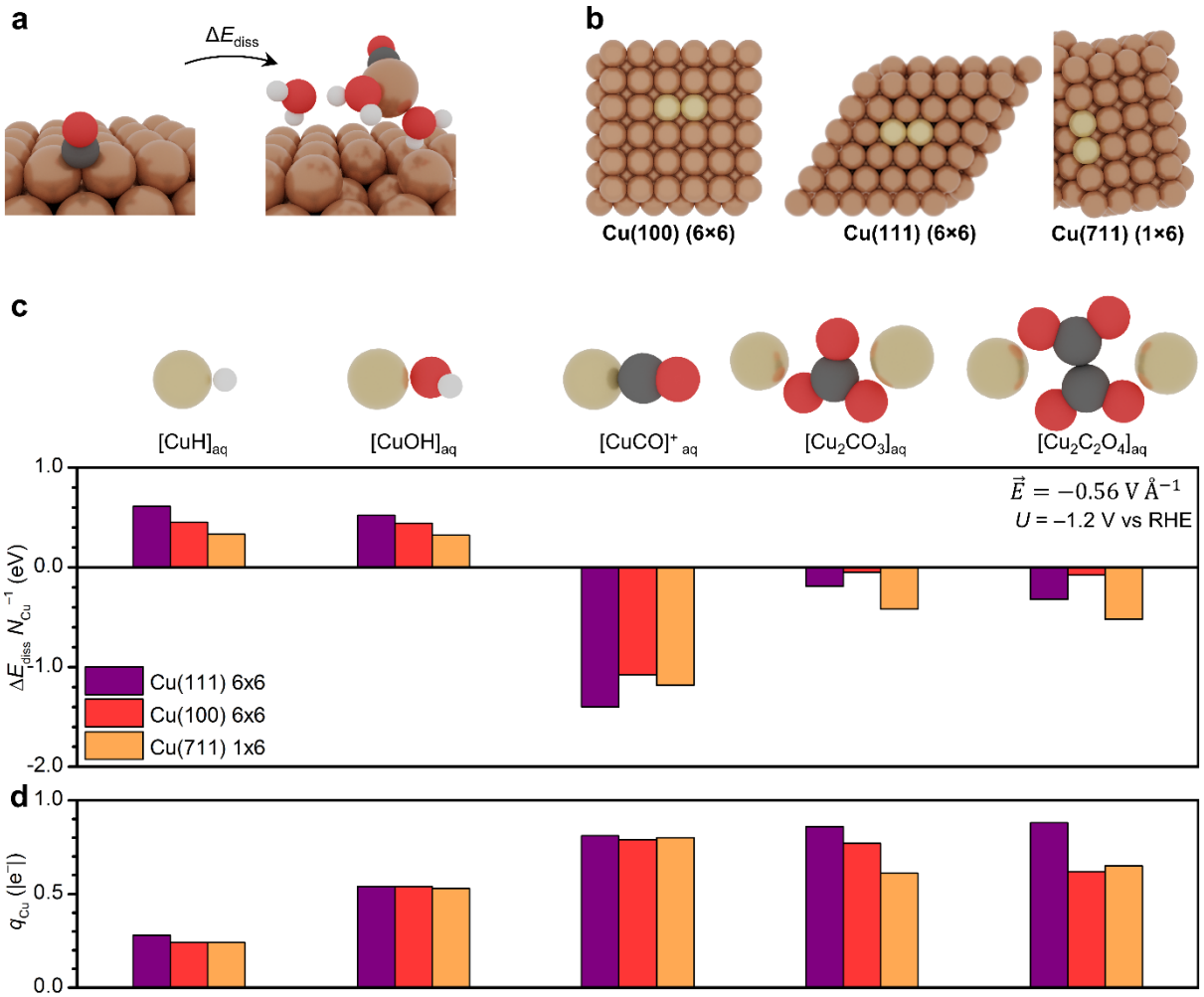

Fig. 5. Adsorbates-driven dissolution of Cu under cathodic bias. (a) Proposed mechanism for the representative case of a copper-carbonyl complex on model step surface Cu(711): first CO_2 reduces to adsorbed CO*, then the $[CuCO]^+$ complex, solvated by H_2O, dissolves in solution (b) DFT models: Cu(100) 6×6, Cu(111) 6×6, and Cu(711) 1×6. Copper atom(s) that are to dissolve in solution are colored in light brown. (c) DFT energy required to desorb $[Cu^+Z]_{aq}$ complexes under an applied electric field of –0.56 V $Å^{-1}$, equivalent to –1.2 V_{RHE} (see Methods). From left to right, Z = H, OH^-, CO, CO_3^{2-}, $C_2O_4^{2-}$. Less favorable species and/or

geometries are reported in Supplementary Fig. S4.2. (d) Average Cu Bader charges for $[Cu^{+}Z]_{aq}$ complexes. Subscript *aq* indicates the presence of one to three H_2O molecules stabilizing each Cu complex.

Once these molecules form or adsorb on the surface, it is reasonable to assume that they desorb as solvated complexes with Cu ion(s), indicated as $[Cu^{+}Z]_{aq}$. To identify the species *Z* which trigger the formation of such $[Cu^{+}Z]_{aq}$ complexes, the DFT energy required for a single Cu surface site to dissolve ($\Delta E_{diss}\, N_{Cu}^{-1}$) was estimated at $U = -1.2$ V_{RHE} (Fig. 5c). The solvated complexes were modeled with one to three H_2O molecules as ligands to reproduce a four-coordination first solvation sphere, while contribution of further shells was modeled through an implicit medium.[49,50] The formation of $[CuH]_{aq}$ and $[CuOH]_{aq}$ is slightly endothermic, which suggest that they only have a minor role in the process. Instead, $[CuCO]^{+}_{aq}$, $[Cu_2C_2O_4]_{aq}$ and $[Cu_2CO_3]_{aq}$ are all thermodynamically favored with the formation of copper-carbonyls and copper-oxalates being the most exothermic. Furthermore, *CO binds more strongly than $*C_2O_4$ and $*CO_3$ at –1.2 V_{RHE} (Supplementary Fig. S4.1), which suggest a higher surface coverage of *CO species under reaction conditions.

All the Cu-*Z* species account for positive Bader charges on the copper atoms, attributable to Cu^{+} oxidation state (Fig. 5d, Supplementary Fig. S4.2, Supplementary Table S4.1), which agrees with the in-situ fluorescence results. It was also observed that dissolution of Cu as $[Cu(phen)_2]^{+}$ is overall less favorable than $[CuCO]^{+}_{aq}$, $[Cu_2C_2O_4]_{aq}$ and $[Cu_2CO_3]_{aq}$ (Supplementary Fig. S4.2). This result suggests that primary dissolved Cu-adsorbate complexes are converted to the phenanthroline complex as a secondary reaction; indeed, energy of the $[CuCO]^{+}$ conversion to $[Cu(phen)_2]^{+}$ is highly exothermic (Supplementary Fig. S3.9). These findings are consistent with the phenanthroline not modifying the mechanism at the copper surface but only facilitating its detection.

Discussion

A final mechanistic picture of the copper dissolution under CO_2RR conditions (Fig. 6) emerges from the experimental and theoretical observations discussed above. The surface adsorption of molecules, including carbon monoxide, carbonate, and oxalate, enables the formation of Cu-adsorbate complexes, which can dissolve in solution. Among these, the formation of $[CuCO]^{+}$ complexes is the most favorable regardless of the Cu surface exposed. Thus, copper carbonyl

complexes identified as the main species driving the dissolution. Nevertheless, these species are short lived in the reaction environment. The $[CuCO]^+$ complex is generally unstable and dissociates to Cu^+ ion and CO(g).[54,55] This mechanism could also explain the previously observed exchange of surface bound CO with dissolved CO, which cannot be described as an adsorption/desorption equilibrium and contribute the accumulation of CO in the close proximity of the Cu catalyst surface.[56,57] Moreover, high local CO concentration has been previously suggested to have detrimental effect on Cu catalyst stability.[12,58] Here the mechanism through which this process occurs is finally elucidated. The redeposition process then occurs via the electrochemical reduction of the released Cu^+ to Cu^0. The dissolution profiles measured in-situ suggest that dissolution and redeposition occur simultaneously. The fast redeposition rate confines the dissolved Cu species in the immediate proximity of the electrode surface. However, gas bubbles were observed to disturb the dissolution-redeposition process and eventually enable long range transport of Cu ions towards the bulk of the electrolyte. This aspect should be considered in assessing the operational stability of CO_2RR electrolyzers operating at high current density, such as gas diffusion electrode setups.

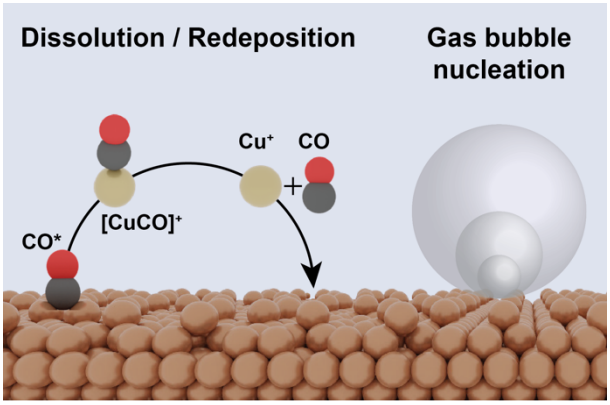

Fig.6: Schematic illustration of the copper reconstruction mechanism under CO_2RR conditions. Adsorbed CO* intermediates drive the transient dissolution followed by redeposition. This process is located to the vicinity of the cathode surface, yet can be perturbed by the nucleation of gaseous reaction products.

As the Cu dissolution in a form of a hydride is unfavorable, the Cu dissolution in the Ar-saturated electrolyte is presumed to result mainly from carbonate adsorption, which has limited surface coverage. The presence of dissolved oxygen and the concomitant ORR is shown to be

detrimental to the Cu catalyst stability. As *OH does not generate stable complexes with copper ions in the modeled environment, the increased Cu dissolution in the air-saturated electrolyte most likely proceeds via a different mechanism, which is out of the scope of this study. However, these results suggest that oxygen presence in the feed CO_2 stream will accelerate Cu catalyst dissolution – redeposition cycle, having detrimental effect on the Cu catalyst stability.

Conclusions

A combination of in-situ techniques was utilized to advance our understanding of the phenomena responsible for Cu catalyst reconstruction during CO_2RR. Evidence for the operational dissolution – redeposition was presented and Cu^+ species were identified as the major reconstruction intermediates under steady state operation. The role of CO_2RR intermediates in this process was further assessed through DFT calculations, including explicit electric field and solvation effects. Copper carbonyls and oxalates were found as the reaction-specific soluble species driving the reconstruction of Cu electrodes during operation.

Operational dissolution – redeposition may be circumvented by developing suitable protection schemes, including porous carbon materials and organic layers.[20,59–61] This study motivates further research in developing schemes which selectively target copper carbonyls and oxalates. Alternatively, the controlled electro (re)deposition of these intermediates to sustain catalyst selectivity and activity over extended time periods should also be considered.

Methods

Catalyst preparation and characterization

The Cu spheres of 7nm and Cu cubes of 44nm were synthesized according to published protocols.[62–64] Glassy carbon sheets were dip-coated in NP suspension, movement of the substrate is controlled via a stepper motor to provide uniform and reproducible nanoparticle films with mass loading of 11 μg cm^{-2} as determined by elemental analysis. Cu foil (99.999%) was electropolished at 3 V for 150s vs Cu foil counter electrode in 70% phosphoric acid. ECSA of prepared electrodes was estimated from a double layer capacitance in the CO_2RR cell, calculated from a CV between –0.2 $V_{Ag/AcCl}$ and –0.15 $V_{Ag/AcCl}$ from the slope of the capacitive current at –0.175 $V_{Ag/AcCl}$ plotted as a function of scan rate between 4 and 32 mV/s.

SEM pictures were acquired with FEI Teneo at 3.0kV. TEM analysis was done either on FEI Spirit at 120 kV or JEOL 2200 FS at 200 kV.

On-line ICP-MS

Cu dissolution was tracked with on-line ICP-MS measurements. The setup consists of an in-house designed and manufactured scanning flow cell (SFC), which outlet was coupled to the inlet of and inductively-coupled plasma mass spectrometer (Perkin Elmer NexION 350X).[23,24] A double junction Ag/AgCl/3M KCl reference electrode (Metrohm) was used as the reference electrode, which was connected to the SFC via a capillary channel on the outlet side of the cell (to avoid Cl^- ion contamination). A glassy carbon rod (SIGRADUR) was applied as the counter electrode, and it was connected to the SFC on the inlet side via a T-connector. Either the freshly polished Cu foil or the spherical Cu NPs-coated glassy carbon electrode served as the working electrode. The NP-coated electrodes were identical to the ones used in the other experiments. The working electrode was placed on an XYZ stage (Physik Instrumente M-403). Electrolyte used is 0.05 M $KHCO_3$ that was saturated either with CO_2 or O_2 as needed. The electrolyte flow (average flow rate was 3.47 μl s^{-1}) was controlled by the peristaltic pump of the ICP-MS (M2, Elemental Scientific). All electrochemical measurements were performed on a Gamry Reference 600 potentiostat. Contact with the electrolyte was established applying -0.28 mA cm-2. After a 600s hold at this current density, four current pulses were applied with gradually decreasing current densities of -0.55 (duration of the hold was 20 s), -1.1 (35s), -2.2 (45s) and -4.4 mA cm^{-2} (55 s). The current density was set back to its baseline value and held there for

120 s after each pulse, except for the last, most negative one, when the current density was left at -0.28 mA cm^{-2} for an additional 800 s. Galvanostatic electrochemical protocol was chosen to allow a better control over bubble formation under CO2RR conditions resulting in more reliable cell operation. For further information about the optimization of measurement protocols see Section 2 in the SI. A custom-developed LabView software was used to control all instruments including the stages, potentiostat, peristaltic pump and gas control box. ICP-MS was calibrated daily by a four-point calibration slope prepared from fresh standard solutions (Cu and Co, Merck Centripur). ^{59}Co served as the internal standard. The internal standard stream was merged with the sample electrolyte stream via a Y-connector before the nebulizer of the ICP-MS.

In-situ fluorescent detection of Cu ions

An H-Cell built in-house was constructed to mimic the typical cells used in CO_2RR catalyst research.[1] The cell geometry defines a 2 mm electrolyte layer between a quartz window and the working electrode. Phenanthroline (1mM) was added to the 0.1M $KHCO_3$ electrolyte and sonicated in a bath sonicator until completely dissolved. Note that the unbound phenanthroline ligands are always in large excess to the generated Cu ions. Electrolyte was pre-saturated with the specified gas, which was then continuously bubbled through the electrolyte during the experiment. Anolyte and catholyte chambers were separated with anion exchange membrane to prevent redeposition of Pt and diffusion of oxygen back to the working electrode. Working electrode was a glassy carbon sheet with 1.5 cm^2 geometric area, signal detection volume was defined by separation of the WE from the quartz window with a gap of 2 mm and beam illuminated area of 3x10 mm in the middle of the WE. Counter electrode was Pt foil (1.5 cm^2) and the used reference electrode was a leak-free Ag/AgCl LF^{-1} from Innovative Instruments Ltd. Bio-Logic SP200 potentiostat was used to bias the electrochemical cell. The potential was converted to RHE scale using Equation 1.

$$E_{RHE}\ (V) = 0.205 + E_{Ag/AgCl} + 0.059*pH \qquad \text{Equation 1}$$

To collect fluorescent spectra, Horiba Jobin Yvon fluorescence spectrometer was used, with excitation wavelength of 400 nm, and detection of phenanthroline fluorescence signal between 415 and 600 nm, 3nm slit width was used for both the excitation and emission monochromators. Recorded counts were normalized to the simultaneously recorded emission intensity.

The fluorescence standards for Cu^{+} and Cu^{2+} were prepared by dissolving 0.5 mM concentration of CuBr or $CuSO_4$ in electrolyte containing 1 mM of phenanthroline. The mixing was performed on a nitrogen Schlenk line to prevent reoxidation of Cu^{+} ions.

The electrochemical cell was continuously bubbled with a gas, typically CO_2 (99.999%). Alternatively N_2 (99.999%) or synthetic air (mixture 79% N_2 and 21% oxygen) was used where specified.

Computational Details

DFT simulations were applied through the Vienna Ab Initio Simulation Package (VASP),[65,66] employing PBE as density functional[48] and van der Waals dispersion through the DFT-D2 method[67,68] with our reparametrized C_6 coefficients.[69] To account for solvent contribution to Cu species formation energy, we employed the VASPsol code.[49,50] Meanwhile, the explicit electric field was included through a dipole correction.[69,70] Electric field was converted to electric potential vs RHE according to Equation 2, where U_{pzc} is the potential of zero charge (vs RHE) and d is the thickness of the electrical double layer, estimated as 3 Å.[71] Since the electric potential applied experimentally (–1.2 V_{RHE}) was beyond the values achievable through DFT simulations, an extrapolation protocol was developed. According to Refs.[20,71] the DFT energy of surfaces and intermediates depends on the electric field through Equation 3. $\vec{p}$ is the electric dipole moment of the intermediate and α its polarizability, while ε is the dielectric permittivity of the medium (electrolyte), A the electrode surface area, and d the thickness of the dielectric double layer. The εAd term indicates the electrostatic energy stored by the surface at cathotic bias, estimated assuming the electrical double layer as a parallel plate capacitor.[20] This hypothesis is valid at the large electrolyte concentrations and large polarization in dilute media characteristic of the experimental conditions.[72] Thus, DFT energies of Cu surfaces, adsorbates, and Cu complexes were calculated for $\vec{E}$ between –0.3 and +0.3 V $Å^{-1}$, and the function $E(\vec{E})$ fitted according to Equation 3 (Supplementary Fig. S4.4). Then, DFT values at –1.2 V vs RHE ($\vec{E}$ = –0.56 V $Å^{-1}$, see Equation 2) were calculated through Equation 3 according to fit parameters (Supplementary Tables S4.2-S4.4).

$$U = U_{\mathrm{pzc}} + \vec{E}d \qquad \text{Equation 2}$$

$$E(\vec{E}) = E(\vec{E} = 0\ \mathrm{V\ Å^{-1}}) + \vec{p}\cdot\vec{E} - \frac{1}{2}(\alpha + \varepsilon Ad)\vec{E}^2 \qquad \text{Equation 3}$$

Inner electrons were represented through PAWpseudopotentials[73,74] and the monoelectronic states corresponding to valence electrons were expanded as plane waves with a kinetic energy cutoff of 450 eV. Three structural models were employed, namely Cu(100) 6×6, Cu(111) 6×6, and Cu(711) 6×6. On as-synthesized Cu nanoparticles, (111) domains are expected to be the most abundant according to Wulff theorem due to their low surface energy,[75] and may evolve to (100) and defective sites, modeled as Cu(711) here, under electrochemical conditions.[6,76] All the crystalline slabs contained at least four equivalent layers, with the two outermost relaxed and the rest fixed to the bulk distances. Vacuum thickness between periodic repetitions of the slabs accounted for at least 15 Å. We sampled the Brillouin zone by a Γ-centered k-points mesh from the Monkhorst-Pack method,[77] with a reciprocal grid size smaller than 0.03 $Å^{-1}$. Each selected Cu-*Z* complexes was set at a distance of more than 3 Å from the surface on one side of the periodic cell, thus we imposed a dipole correction to correct artifacts from the asymmetric slab model.[78] We reported all formation energies using CO_2(g), H_2(g), H_2O(g), phenanthroline(g) and the clean surface as energy references. When needed, CO(g) energy was estimated from DFT and experimental values following the procedure described in Ref.[79]

Data availability

The datasets generated though DFT and analysed during the current study are available in the ioChem-BD database[80] at DOI 10.19061/iochem-bd-1-231, currently under embargo. Reviewers can access the full dataset here: https://iochem-bd.iciq.es/browse/review-collection/100/36205/23ee811de59d952e37462864. Experimental data are available from the authors upon reasonable request.

References

(1) Nitopi, S.; Bertheussen, E.; Scott, S. B.; Liu, X.; Engstfeld, A. K.; Horch, S.; Seger, B.; Stephens, I. E. L.; Chan, K.; Hahn, C.; Nørskov, J. K.; Jaramillo, T. F.; Chorkendorff, I. Progress and Perspectives of Electrochemical CO_2 Reduction on Copper in Aqueous Electrolyte. *Chem. Rev.* **2019**, *119* (12), 7610–7672. https://doi.org/10.1021/acs.chemrev.8b00705.

(2) Huang, J.; Buonsanti, R. Colloidal Nanocrystals as Heterogeneous Catalysts for Electrochemical CO2 Conversion. *Chem. Mater.* **2019**, *31* (1), 13–25. https://doi.org/10.1021/acs.chemmater.8b04155.

(3) Hahn, C.; Hatsukade, T.; Kim, Y.-G.; Vailionis, A.; Baricuatro, J. H.; Higgins, D. C.; Nitopi, S. A.; Soriaga, M. P.; Jaramillo, T. F. Engineering Cu Surfaces for the Electrocatalytic Conversion of CO_2: Controlling Selectivity toward Oxygenates and Hydrocarbons. *Proc. Natl. Acad. Sci.* **2017**, *114* (23), 5918–5923. https://doi.org/10.1073/pnas.1618935114.

(4) Seh, Z. W.; Kibsgaard, J.; Dickens, C. F.; Chorkendorff, I.; Nørskov, J. K.; Jaramillo, T. F. Combining Theory and Experiment in Electrocatalysis: Insights into Materials Design. *Science* **2017**, *355* (6321), eaad4998. https://doi.org/10.1126/science.aad4998.

(5) Schouten, K. J. P.; Pérez Gallent, E.; Koper, M. T. M. Structure Sensitivity of the Electrochemical Reduction of Carbon Monoxide on Copper Single Crystals. *ACS Catal.* **2013**, *3* (6), 1292–1295. https://doi.org/10.1021/cs4002404.

(6) Kim, Y.-G.; Baricuatro, J. H.; Javier, A.; Gregoire, J. M.; Soriaga, M. P. The Evolution of the Polycrystalline Copper Surface, First to Cu(111) and Then to Cu(100), at a Fixed CO_2 RR Potential: A Study by *Operando* EC-STM. *Langmuir* **2014**, *30* (50), 15053–15056. https://doi.org/10.1021/la504445g.

(7) Manthiram, K.; Beberwyck, B. J.; Alivisatos, A. P. Enhanced Electrochemical Methanation of Carbon Dioxide with a Dispersible Nanoscale Copper Catalyst. *J. Am. Chem. Soc.* **2014**, *136* (38), 13319–13325. https://doi.org/10.1021/ja5065284.

(8) Gunathunge, C. M.; Li, X.; Li, J.; Hicks, R. P.; Ovalle, V. J.; Waegele, M. M. Spectroscopic Observation of Reversible Surface Reconstruction of Copper Electrodes under CO_2 Reduction. *J. Phys. Chem. C* **2017**, *121* (22), 12337–12344. https://doi.org/10.1021/acs.jpcc.7b03910.

(9) Kim, D.; Kley, C. S.; Li, Y.; Yang, P. Copper Nanoparticle Ensembles for Selective Electroreduction of CO_2 to C_2–C_3 Products. *Proc. Natl. Acad. Sci.* **2017**, *114* (40), 10560–10565. https://doi.org/10.1073/pnas.1711493114.

(10) Grosse, P.; Gao, D.; Scholten, F.; Sinev, I.; Mistry, H.; Roldan Cuenya, B. Dynamic Changes in the Structure, Chemical State and Catalytic Selectivity of Cu Nanocubes during CO_2 Electroreduction: Size and Support Effects. *Angew. Chem. Int. Ed.* **2018**, *57* (21), 6192–6197. https://doi.org/10.1002/anie.201802083.

(11) Huang, J.; Hörmann, N.; Oveisi, E.; Loiudice, A.; De Gregorio, G. L.; Andreussi, O.; Marzari, N.; Buonsanti, R. Potential-Induced Nanoclustering of Metallic Catalysts during Electrochemical CO2 Reduction. *Nat. Commun.* **2018**, *9* (1), 3117. https://doi.org/10.1038/s41467-018-05544-3.

(12) Osowiecki, W. T.; Nussbaum, J. J.; Kamat, G. A.; Katsoukis, G.; Ledendecker, M.; Frei, H.; Bell, A. T.; Alivisatos, A. P. Factors and Dynamics of Cu Nanocrystal Reconstruction under CO_2 Reduction. *ACS Appl. Energy Mater.* **2019**, *2* (11), 7744–7749. https://doi.org/10.1021/acsaem.9b01714.

(13) Jung, H.; Lee, S. Y.; Lee, C. W.; Cho, M. K.; Won, D. H.; Kim, C.; Oh, H.-S.; Min, B. K.; Hwang, Y. J. Electrochemical Fragmentation of Cu2O Nanoparticles Enhancing

Selective C–C Coupling from CO2 Reduction Reaction. *J. Am. Chem. Soc.* **2019**, *141* (11), 4624–4633. https://doi.org/10.1021/jacs.8b11237.
(14) Vavra, J.; Shen, T.-H.; Stoian, D.; Tileli, V.; Buonsanti, R. Real-Time Monitoring Reveals Dissolution/Redeposition Mechanism in Copper Nanocatalysts during the Initial Stages of the CO2 Reduction Reaction. *Angew. Chem. Int. Ed.* **2021**, *60* (3), 1347–1354. https://doi.org/10.1002/anie.202011137.
(15) Raaijman, S. J.; Arulmozhi, N.; Koper, M. T. M. Morphological Stability of Copper Surfaces under Reducing Conditions. *ACS Appl. Mater. Interfaces* **2021**, acsami.1c13989. https://doi.org/10.1021/acsami.1c13989.
(16) Popovic, S.; Bele, M.; Hodnik, N. Reconstruction of Copper Nanoparticles at Electrochemical CO $_2$ Reduction Reaction Conditions Occurs *via* Two-step Dissolution/Redeposition Mechanism. *ChemElectroChem* **2021**, *8* (14), 2634–2639. https://doi.org/10.1002/celc.202100387.
(17) Speck, F. D.; Cherevko, S. Electrochemical Copper Dissolution: A Benchmark for Stable CO2 Reduction on Copper Electrocatalysts. *Electrochem. Commun.* **2020**, *115*, 106739. https://doi.org/10.1016/j.elecom.2020.106739.
(18) Hochfilzer, D.; Sørensen, J. E.; Clark, E. L.; Scott, S. B.; Chorkendorff, I.; Kibsgaard, J. The Importance of Potential Control for Accurate Studies of Electrochemical CO Reduction. *ACS Energy Lett.* **2021**, *6* (5), 1879–1885. https://doi.org/10.1021/acsenergylett.1c00496.
(19) Lee, S. H.; Lin, J. C.; Farmand, M.; Landers, A. T.; Feaster, J. T.; Avilés Acosta, J. E.; Beeman, J. W.; Ye, Y.; Yano, J.; Mehta, A.; Davis, R. C.; Jaramillo, T. F.; Hahn, C.; Drisdell, W. S. Oxidation State and Surface Reconstruction of Cu under CO2 Reduction Conditions from In Situ X-Ray Characterization. *J. Am. Chem. Soc.* **2021**, *143* (2), 588–592. https://doi.org/10.1021/jacs.0c10017.
(20) Phan, T. H.; Banjac, K.; Cometto, F. P.; Dattila, F.; García-Muelas, R.; Raaijman, S. J.; Ye, C.; Koper, M. T. M.; López, N.; Lingenfelder, M. Emergence of Potential-Controlled Cu-Nanocuboids and Graphene-Covered Cu-Nanocuboids under Operando CO2 Electroreduction. *Nano Lett.* **2021**, *21* (5), 2059–2065. https://doi.org/10.1021/acs.nanolett.0c04703.
(21) Simon, G. H.; Kley, C. S.; Roldan Cuenya, B. Potential-Dependent Morphology of Copper Catalysts During CO $_2$ Electroreduction Revealed by In Situ Atomic Force Microscopy. *Angew. Chem. Int. Ed.* **2021**, *60* (5), 2561–2568. https://doi.org/10.1002/anie.202010449.
(22) Li, Y.; Kim, D.; Louisia, S.; Xie, C.; Kong, Q.; Yu, S.; Lin, T.; Aloni, S.; Fakra, S. C.; Yang, P. Electrochemically Scrambled Nanocrystals Are Catalytically Active for CO2-to-Multicarbons. *Proc. Natl. Acad. Sci.* **2020**, *117* (17), 9194–9201. https://doi.org/10.1073/pnas.1918602117.
(23) Kasian, O.; Geiger, S.; Mayrhofer, K. J. J.; Cherevko, S. Electrochemical On-Line ICP-MS in Electrocatalysis Research. *Chem. Rec.* **2019**, *19* (10), 2130–2142. https://doi.org/10.1002/tcr.201800162.
(24) Cherevko, S.; Kulyk, N.; Mayrhofer, K. J. J. Durability of Platinum-Based Fuel Cell Electrocatalysts: Dissolution of Bulk and Nanoscale Platinum. *Nano Energy* **2016**, *29*, 275–298. https://doi.org/10.1016/j.nanoen.2016.03.005.
(25) Cherevko, S. Electrochemical Dissolution of Noble Metals Native Oxides. *J. Electroanal. Chem.* **2017**, *787*, 11–13. https://doi.org/10.1016/j.jelechem.2017.01.029.
(26) Pallenberg, A. J.; Koenig, K. S.; Barnhart, D. M. Synthesis and Characterization of Some Copper(I) Phenanthroline Complexes. *Inorg. Chem.* **1995**, *34* (11), 2833–2840. https://doi.org/10.1021/ic00115a009.

(27) Armaroli, N. Photoactive Mono- and Polynuclear Cu(i)–Phenanthrolines. A Viable Alternative to Ru(Ii)–Polypyridines? *Chem. Soc. Rev.* **2001**, *30* (2), 113–124. https://doi.org/10.1039/b000703j.
(28) Wang, J.; Gan, L.; Zhang, Q.; Reddu, V.; Peng, Y.; Liu, Z.; Xia, X.; Wang, C.; Wang, X. A Water-Soluble Cu Complex as Molecular Catalyst for Electrocatalytic CO2 Reduction on Graphene-Based Electrodes. *Adv. Energy Mater.* **2019**, *9* (3), 1803151. https://doi.org/10.1002/aenm.201803151.
(29) Fahrni, C. J. Synthetic Fluorescent Probes for Monovalent Copper. *Curr. Opin. Chem. Biol.* **2013**, *17* (4), 656–662. https://doi.org/10.1016/j.cbpa.2013.05.019.
(30) Price, K. A.; Hickey, J. L.; Xiao, Z.; Wedd, A. G.; James, S. A.; Liddell, J. R.; Crouch, P. J.; White, A. R.; Donnelly, P. S. The Challenges of Using a Copper Fluorescent Sensor (CS1) to Track Intracellular Distributions of Copper in Neuronal and Glial Cells. *Chem. Sci.* **2012**, *3* (9), 2748–2759. https://doi.org/10.1039/C2SC20397A.
(31) Taki, M.; Iyoshi, S.; Ojida, A.; Hamachi, I.; Yamamoto, Y. Development of Highly Sensitive Fluorescent Probes for Detection of Intracellular Copper(I) in Living Systems. *J. Am. Chem. Soc.* **2010**, *132* (17), 5938–5939. https://doi.org/10.1021/ja100714p.
(32) Garg, S.; Li, M.; Weber, A. Z.; Ge, L.; Li, L.; Rudolph, V.; Wang, G.; Rufford, T. E. Advances and Challenges in Electrochemical CO2 Reduction Processes: An Engineering and Design Perspective Looking beyond New Catalyst Materials. *J. Mater. Chem. A* **2020**, *8* (4), 1511–1544. https://doi.org/10.1039/C9TA13298H.
(33) Sangeetha, S.; Sathyaraj, G.; Muthamilselvan, D.; Vaidyanathan, V. G.; Nair, B. U. Structurally Modified 1,10-Phenanthroline Based Fluorophores for Specific Sensing of Ni2+ and Cu2+ Ions. *Dalton Trans.* **2012**, *41* (19), 5769–5773. https://doi.org/10.1039/C2DT30525A.
(34) Ma, X. A Phenanthroline-Based Fluorescent Probe for Highly Selective Detection of Extreme Alkalinity (PH > 14) in Aqueous Solution. **2019**, 10.
(35) Yang, K.; Kas, R.; Smith, W. A. In Situ Infrared Spectroscopy Reveals Persistent Alkalinity near Electrode Surfaces during CO2 Electroreduction. *J. Am. Chem. Soc.* **2019**, *141* (40), 15891–15900. https://doi.org/10.1021/jacs.9b07000.
(36) Velasco-Vélez, J.-J.; Jones, T.; Gao, D.; Carbonio, E.; Arrigo, R.; Hsu, C.-J.; Huang, Y.-C.; Dong, C.-L.; Chen, J.-M.; Lee, J.-F.; Strasser, P.; Roldan Cuenya, B.; Schlögl, R.; Knop-Gericke, A.; Chuang, C.-H. The Role of the Copper Oxidation State in the Electrocatalytic Reduction of CO2 into Valuable Hydrocarbons. *ACS Sustain. Chem. Eng.* **2019**, *7* (1), 1485–1492. https://doi.org/10.1021/acssuschemeng.8b05106.
(37) Dattila, F.; García-Muelas, R.; López, N. Active and Selective Ensembles in Oxide-Derived Copper Catalysts for CO2 Reduction. *ACS Energy Lett.* **2020**, *5* (10), 3176–3184. https://doi.org/10.1021/acsenergylett.0c01777.
(38) McCrum, I. T.; Bondue, C. J.; Koper, M. T. M. Hydrogen-Induced Step-Edge Roughening of Platinum Electrode Surfaces. *J. Phys. Chem. Lett.* **2019**, *10* (21), 6842–6849. https://doi.org/10.1021/acs.jpclett.9b02544.
(39) Hersbach, T. J. P.; Koper, M. T. M. Cathodic Corrosion: 21st Century Insights into a 19th Century Phenomenon. *Curr. Opin. Electrochem.* **2021**, *26*, 100653. https://doi.org/10.1016/j.coelec.2020.100653.
(40) Kreizer, I. V.; Tutukina, N. M.; Zartsyn, I. D.; Marshakov, I. K. The Dissolution of a Copper Cathode in Acidic Chloride Solutions. **2002**, *38* (3), 7.
(41) Kreizer, I. V.; Marshakov, I. K.; Tutukina, N. M.; Zartsyn, I. D. Partial Reactions of Copper Dissolution under Cathodic Polarization in Acidic Media. *Prot. Met.* **2004**, *40* (1), 23–25. https://doi.org/10.1023/B:PROM.0000013107.65745.b0.
(42) Kreizer, V.; Marshakov, I. K.; Tutukina, N. M.; Zartsyn, I. D. The Effect of Oxygen on Copper Dissolution during Cathodic Polarization. **2003**, *39* (1), 4.

(43) Ross, M. B.; De Luna, P.; Li, Y.; Dinh, C.-T.; Kim, D.; Yang, P.; Sargent, E. H. Designing Materials for Electrochemical Carbon Dioxide Recycling. *Nat. Catal.* **2019**, *2* (8), 648–658. https://doi.org/10.1038/s41929-019-0306-7.
(44) Cave, E. R.; Shi, C.; Kuhl, K. P.; Hatsukade, T.; Abram, D. N.; Hahn, C.; Chan, K.; Jaramillo, T. F. Trends in the Catalytic Activity of Hydrogen Evolution during CO2 Electroreduction on Transition Metals. *ACS Catal.* **2018**, *8* (4), 3035–3040. https://doi.org/10.1021/acscatal.7b03807.
(45) Zhou, H.; Xiong, B.; Chen, L.; Shi, J. Modulation Strategies of Cu-Based Electrocatalysts for Efficient Nitrogen Reduction. *J. Mater. Chem. A* **2020**, *8* (39), 20286–20293. https://doi.org/10.1039/D0TA06776H.
(46) Xu, Y.; Edwards, J. P.; Zhong, J.; O'Brien, C. P.; Gabardo, C. M.; McCallum, C.; Li, J.; Dinh, C.-T.; Sargent, E. H.; Sinton, D. Oxygen-Tolerant Electroproduction of C2 Products from Simulated Flue Gas. *Energy Environ. Sci.* **2020**, *13* (2), 554–561. https://doi.org/10.1039/C9EE03077H.
(47) Qaseem, A.; Chen, F.; Wu, X.; Johnston, R. L. Pt-Free Silver Nanoalloy Electrocatalysts for Oxygen Reduction Reaction in Alkaline Media. *Catal. Sci. Technol.* **2016**, *6* (10), 3317–3340. https://doi.org/10.1039/C5CY02270C.
(48) Perdew, J. P.; Burke, K.; Ernzerhof, M. Generalized Gradient Approximation Made Simple. *Phys. Rev. Lett.* **1996**, *77* (18), 3865–3868. https://doi.org/10.1103/PhysRevLett.77.3865.
(49) Fishman, M.; Zhuang, H. L.; Mathew, K.; Dirschka, W.; Hennig, R. G. Accuracy of Exchange-Correlation Functionals and Effect of Solvation on the Surface Energy of Copper. *Phys. Rev. B* **2013**, *87* (24), 245402. https://doi.org/10.1103/PhysRevB.87.245402.
(50) Mathew, K.; Sundararaman, R.; Letchworth-Weaver, K.; Arias, T. A.; Hennig, R. G. Implicit Solvation Model for Density-Functional Study of Nanocrystal Surfaces and Reaction Pathways. *J. Chem. Phys.* **2014**, *140* (8), 084106. https://doi.org/10.1063/1.4865107.
(51) Calle-Vallejo, F.; Martínez, J. I.; García-Lastra, J. M.; Sautet, P.; Loffreda, D. Fast Prediction of Adsorption Properties for Platinum Nanocatalysts with Generalized Coordination Numbers. *Angew. Chem. Int. Ed.* **2014**, *53* (32), 8316–8319. https://doi.org/10.1002/anie.201402958.
(52) Calle-Vallejo, F.; Tymoczko, J.; Colic, V.; Vu, Q. H.; Pohl, M. D.; Morgenstern, K.; Loffreda, D.; Sautet, P.; Schuhmann, W.; Bandarenka, A. S. Finding Optimal Surface Sites on Heterogeneous Catalysts by Counting Nearest Neighbors. *Science* **2015**. https://doi.org/10.1126/science.aab3501.
(53) Calle-Vallejo, F.; Loffreda, D.; Koper, M. T. M.; Sautet, P. Introducing Structural Sensitivity into Adsorption–Energy Scaling Relations by Means of Coordination Numbers. *Nat. Chem.* **2015**, *7* (5), 403–410. https://doi.org/10.1038/nchem.2226.
(54) Pasquali, M.; Floriani, C.; Gaetani-Manfredotti, A. Carbon Monoxide Absorption by Copper(I) Halides in Organic Solvents: Isolation and Structure of .Mu.-Halogeno-Dicopper(I) Carbonyl Complexes. *Inorg. Chem.* **1981**, *20* (10), 3382–3388. https://doi.org/10.1021/ic50224a046.
(55) Pike, R. D. Structure and Bonding in Copper(I) Carbonyl and Cyanide Complexes. *Organometallics* **2012**, *31* (22), 7647–7660. https://doi.org/10.1021/om3004459.
(56) Wuttig, A.; Liu, C.; Peng, Q.; Yaguchi, M.; Hendon, C. H.; Motobayashi, K.; Ye, S.; Osawa, M.; Surendranath, Y. Tracking a Common Surface-Bound Intermediate during CO2-to-Fuels Catalysis. *ACS Cent. Sci.* **2016**, *2* (8), 522–528. https://doi.org/10.1021/acscentsci.6b00155.

(57) Clark, E. L.; Bell, A. T. Direct Observation of the Local Reaction Environment during the Electrochemical Reduction of CO2. *J. Am. Chem. Soc.* **2018**, *140* (22), 7012–7020. https://doi.org/10.1021/jacs.8b04058.
(58) Wilde, P.; O'Mara, P. B.; Junqueira, J. R. C.; Tarnev, T.; Benedetti, T. M.; Andronescu, C.; Chen, Y.-T.; Tilley, R. D.; Schuhmann, W.; Gooding, J. J. Is Cu Instability during the CO $_2$ Reduction Reaction Governed by the Applied Potential or the Local CO Concentration? *Chem. Sci.* **2021**, *12* (11), 4028–4033. https://doi.org/10.1039/D0SC05990K.
(59) Li, Y.; Cui, F.; Ross, M. B.; Kim, D.; Sun, Y.; Yang, P. Structure-Sensitive CO2 Electroreduction to Hydrocarbons on Ultrathin 5-Fold Twinned Copper Nanowires. *Nano Lett.* **2017**, *17* (2), 1312–1317. https://doi.org/10.1021/acs.nanolett.6b05287.
(60) Zhang, L.; Wei, Z.; Thanneeru, S.; Meng, M.; Kruzyk, M.; Ung, G.; Liu, B.; He, J. A Polymer Solution To Prevent Nanoclustering and Improve the Selectivity of Metal Nanoparticles for Electrocatalytic CO2 Reduction. *Angew. Chem. Int. Ed.* **2019**, *58* (44), 15834–15840. https://doi.org/10.1002/anie.201909069.
(61) He, J.; Huang, A.; Johnson, N. J. J.; Dettelbach, K. E.; Weekes, D. M.; Cao, Y.; Berlinguette, C. P. Stabilizing Copper for CO2 Reduction in Low-Grade Electrolyte. *Inorg. Chem.* **2018**, *57* (23), 14624–14631. https://doi.org/10.1021/acs.inorgchem.8b02311.
(62) Gadiyar, C.; Strach, M.; Schouwink, P.; Loiudice, A.; Buonsanti, R. Chemical Transformations at the Nanoscale: Nanocrystal-Seeded Synthesis of β-Cu $_2$ V $_2$ O $_7$ with Enhanced Photoconversion Efficiencies. *Chem. Sci.* **2018**, *9* (25), 5658–5665. https://doi.org/10.1039/C8SC01314D.
(63) Hung, L.-I.; Tsung, C.-K.; Huang, W.; Yang, P. Room-Temperature Formation of Hollow Cu2O Nanoparticles. *Adv. Mater.* **2010**, *22* (17), 1910–1914. https://doi.org/10.1002/adma.200903947.
(64) Loiudice, A.; Lobaccaro, P.; Kamali, E. A.; Thao, T.; Huang, B. H.; Ager, J. W.; Buonsanti, R. Tailoring Copper Nanocrystals towards C2 Products in Electrochemical CO2 Reduction. *Angew. Chem. Int. Ed.* **2016**, *55* (19), 5789–5792. https://doi.org/10.1002/anie.201601582.
(65) Kresse, G.; Furthmüller, J. Efficiency of Ab-Initio Total Energy Calculations for Metals and Semiconductors Using a Plane-Wave Basis Set. *Comput. Mater. Sci.* **1996**, *6* (1), 15–50. https://doi.org/10.1016/0927-0256(96)00008-0.
(66) Kresse, G.; Furthmüller, J. Efficient Iterative Schemes for Ab Initio Total-Energy Calculations Using a Plane-Wave Basis Set. *Phys. Rev. B* **1996**, *54* (16), 11169–11186. https://doi.org/10.1103/PhysRevB.54.11169.
(67) Grimme, S. Semiempirical GGA-Type Density Functional Constructed with a Long-Range Dispersion Correction. *J. Comput. Chem.* **2006**, *27* (15), 1787–1799. https://doi.org/10.1002/jcc.20495.
(68) Bučko, T.; Hafner, J.; Lebègue, S.; Ángyán, J. G. Improved Description of the Structure of Molecular and Layered Crystals: Ab Initio DFT Calculations with van Der Waals Corrections. *J. Phys. Chem. A* **2010**, *114* (43), 11814–11824. https://doi.org/10.1021/jp106469x.
(69) Almora-Barrios, N.; Carchini, G.; Błoński, P.; López, N. Costless Derivation of Dispersion Coefficients for Metal Surfaces. *J. Chem. Theory Comput.* **2014**, *10* (11), 5002–5009. https://doi.org/10.1021/ct5006467.
(70) Feibelman, P. J. Surface-Diffusion Mechanism versus Electric Field: Pt/Pt(001). *Phys. Rev. B* **2001**, *64* (12), 125403. https://doi.org/10.1103/PhysRevB.64.125403.

(71) Chen, L. D.; Urushihara, M.; Chan, K.; Nørskov, J. K. Electric Field Effects in Electrochemical CO2 Reduction. *ACS Catal.* **2016**, *6* (10), 7133–7139. https://doi.org/10.1021/acscatal.6b02299.
(72) Bard, A. J.; Faulkner, L. R. *Electrochemical Methods: Fundamentals and Applications*, 2nd Edition.; Wiley.
(73) Blöchl, P. E. Projector Augmented-Wave Method. *Phys. Rev. B* **1994**, *50* (24), 17953–17979. https://doi.org/10.1103/PhysRevB.50.17953.
(74) Kresse, G.; Joubert, D. From Ultrasoft Pseudopotentials to the Projector Augmented-Wave Method. *Phys. Rev. B* **1999**, *59* (3), 1758–1775. https://doi.org/10.1103/PhysRevB.59.1758.
(75) Wulff, G. XXV. Zur Frage der Geschwindigkeit des Wachsthums und der Auflösung der Krystallflächen. *Z. Für Krist. - Cryst. Mater.* **1901**, *34* (1–6), 449–530. https://doi.org/10.1524/zkri.1901.34.1.449.
(76) Kim, Y.-G.; Javier, A.; Baricuatro, J. H.; Torelli, D.; Cummins, K. D.; Tsang, C. F.; Hemminger, J. C.; Soriaga, M. P. Surface Reconstruction of Pure-Cu Single-Crystal Electrodes under CO-Reduction Potentials in Alkaline Solutions: A Study by Seriatim ECSTM-DEMS. *J. Electroanal. Chem.* **2016**, *780*, 290–295. https://doi.org/10.1016/j.jelechem.2016.09.029.
(77) Monkhorst, H. J.; Pack, J. D. Special Points for Brillouin-Zone Integrations. *Phys. Rev. B* **1976**, *13* (12), 5188–5192. https://doi.org/10.1103/PhysRevB.13.5188.
(78) Makov, G.; Payne, M. C. Periodic Boundary Conditions in Ab Initio Calculations. *Phys. Rev. B* **1995**, *51* (7), 4014–4022. https://doi.org/10.1103/PhysRevB.51.4014.
(79) Granda-Marulanda, L. P.; Rendón-Calle, A.; Builes, S.; Illas, F.; Koper, M. T. M.; Calle-Vallejo, F. A Semiempirical Method to Detect and Correct DFT-Based Gas-Phase Errors and Its Application in Electrocatalysis. *ACS Catal.* **2020**, *10* (12), 6900–6907. https://doi.org/10.1021/acscatal.0c01075.
(80) Álvarez-Moreno, M.; de Graaf, C.; López, N.; Maseras, F.; Poblet, J. M.; Bo, C. Managing the Computational Chemistry Big Data Problem: The IoChem-BD Platform. *J. Chem. Inf. Model.* **2015**, *55* (1), 95–103. https://doi.org/10.1021/ci500593j.